A New Wavelet Transform and Merging Generative Adversarial Network (WTM-GAN) Model for TEC Spatial Inpainting

Kunlin Yang , Yang Liu, Yifei Chen, Zhizhao Liu, *Member, IEEE*, Kaiyan Jin, and Yanbo Zhu, *Member, IEEE*

Abstract-Due to the uneven distribution of ground observatories, the effective data coverage of global ionospheric TEC is below 50%. The International GNSS Service provides a global ionosphere map based on a single shell assumption, derived from the ground-based observations. This serves as the main reference for global ionosphere morphology study. In this work, a new GAN model, wavelet transform and merging generative adversarial network (WTM-GAN) is proposed, designed for spatial completion of ionospheric TEC data with observation coverage deficiency. WTM-GAN is designed with an encoder-decoder architecture, using a Haar wavelet filter and a multilayer decoder employing segmentation and merging techniques. The performance is rigorously tested, achieving root-mean-square errors of 2.117 TECu and 0.908 TECu during both high and low solar activity years, respectively, and it obtains improvement of 0.945 TECu and 0.739 TECu over the comparison models. It also attained a peak signal-to-noise ratio over 32 dB, outperforming all comparisons. During geomagnetic storms, WTM-GAN effectively captures features in the equatorial ionization anomaly region, demonstrating enhanced spatial observation augmentation accuracy and stability. This framework offers a robust solution for TEC data completion, improving the reliability of ionospheric studies.

Index Terms—Generative adversarial network (GAN), ionosphere, spatial inpainting, total electron content (TEC).

I. INTRODUCTION

HE ionosphere serves as an essential part of the Earth's atmosphere, playing a critical role as a medium for transionosphere radio propagation. It consists of the partially ionized neutral atmosphere, which is influenced by solar radiation and geomagnetic modulation [1], [2], [3], [4], [5]. The radio signals passing through the ionosphere suffer from reflection

Received 8 April 2025; revised 20 June 2025 and 8 July 2025; accepted 15 July 2025. Date of publication 22 July 2025; date of current version 22 August 2025. This work was supported in part by the National Key Research and Development Plan and in part by Ministry of Science and Technology under Grant 2022YFB3904302. (Corresponding author: Yang Liu.)

Kunlin Yang, Yang Liu, and Yifei Chen are with the School of Instrumentation and Optoelectronic Engineering, Beihang University, Beijing 100191, P.R. China (e-mail: yangkunlin@buaa.edu.cn; liuyangee@buaa.edu.cn; zy2317119@buaa.edu.cn).

Zhizhao Liu is with the Department of Land Surveying and Geo-Informatics, The Hong Kong Polytechnic University, Hung Hom, Kowloon, Hong Kong, P.R. China (e-mail: george.liu@polyu.edu.hk).

Kaiyan Jin and Yanbo Zhu are with the School of Electronic Information Engineering, Beihang University, Beijing 100191, P.R. China, and also with the Aviation Data Communication Corporation, China and State Key Laboratory of CNS/ATM, Beijing 100191, P.R. China (e-mail: jinky@adcc.com.cn; zyb@adcc.com.cn).

Digital Object Identifier 10.1109/JSTARS.2025.3591103

and refraction, affecting airspace communication and satellite navigations [6], [7], [8], [9], [10], [11].

The correction of ionospheric delay requires accurate calculation for the total electron content (TEC) in the ionosphere. Since 1998, the Massachusetts Institute of Technology (MIT) has been collecting ground-based global navigation satellite system (GNSS) observations from over 6000 stations and then calculating TEC data, providing the MIT-TEC product for the study of the ionosphere [12], [13]. The MIT-TEC data is one of the most popularly applied TEC data derived from ground observations, but it does not provide global coverage due to limitation of ground deployed stations [14]. In particular, there is a significant lack of data in regions such as oceans and polar areas. The available data accounts for approximately 30%–48%, and the data gaps further hinder the study of the global morphology and variations in the ionosphere [15]. To address the problem, it is necessary to generate finer global ionosphere TEC morphology in spatio-temporal resolutions.

The International GNSS Service (IGS) currently provides global ionospheric map (GIM) products by the IGS ionosphere associate analysis centers. The most commonly used GIM product is in two hours interval, with a spatial resolution of 2.5° in latitude 5° in longitude. Since 2000, IGS-GIM products maintain a continuous temporal data storage for over twenty years, serving as a solid data source for the global ionosphere investigations. A great amount of ionosphere studies, including the geomagnetic storm response, the equatorial ionization anomaly features as well as the spatio-temporal variation in different scales are based on the GIM products [16], [17], [18], [19], [20], [21], [22], [23].

The recent development of deep learning techniques has shed light on the spatio-temporal estimation and prediction in ionosphere TEC [22], [24], [25], [26], [27], [28], [29], [30], [31]. For instance, Chen et al. [32] developed a regularized-DCGAN (R-DCGAN) network. Ji et al. [33] introduced the Deep-IRI model with conditional GANs. It successfully reconstructed ionospheric peak structures and improved the accuracy of the IRI-TEC in the EIA region. It incorporated existing IGS-GIM products as additional references to generate ionospheric peak features under various time and geomagnetic conditions. Subsequently, Pan et al. [34] proposed the DCGAN-PB framework, which employed Poisson blending to make further smoothness for image fusion. This model automatically completed global TEC maps and accurately restored missing data while

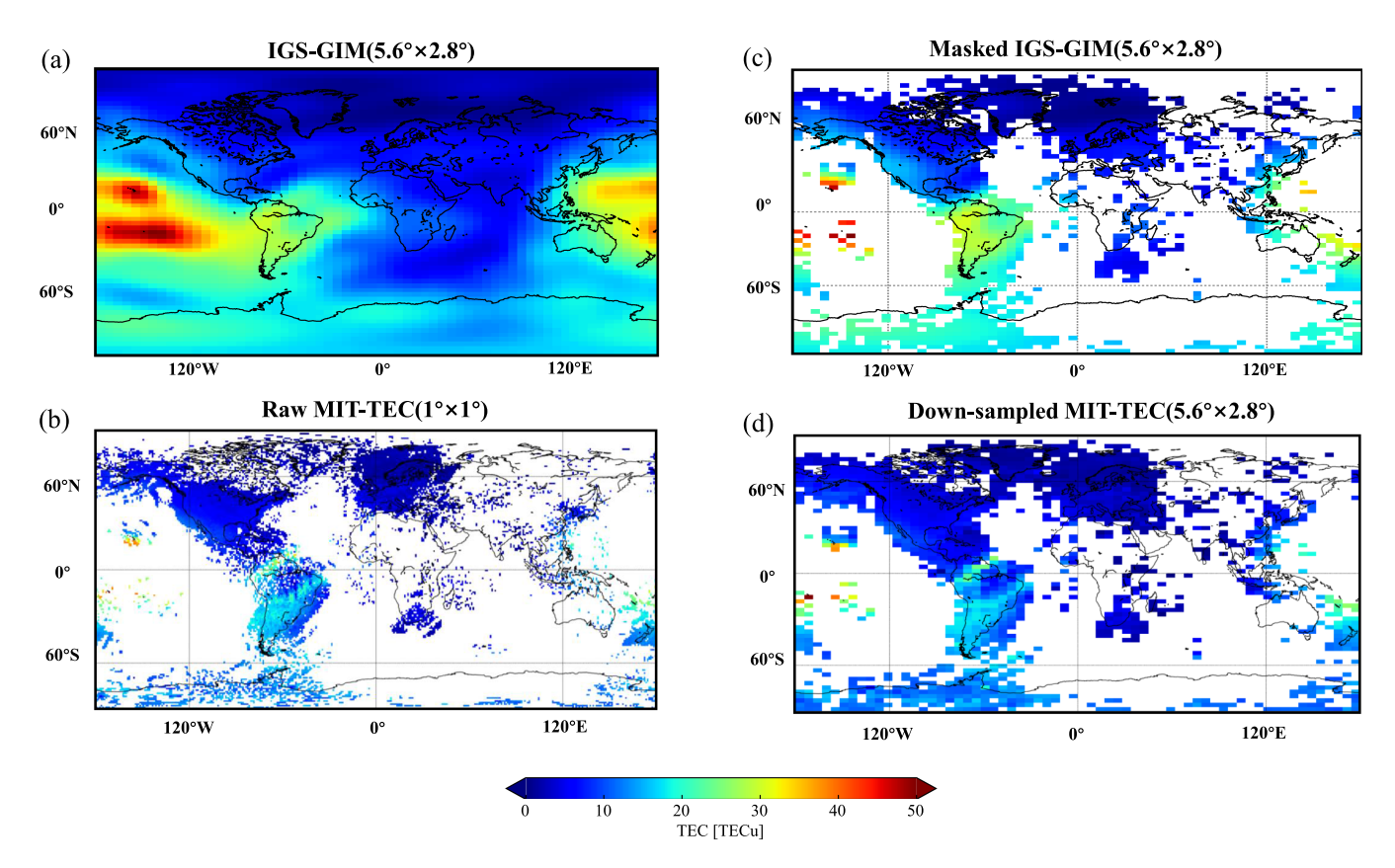


Fig. 1. Original data and postprocessing of MIT-TEC and IGS-GIM (Take 00:00UT on 1 January 2022, as an example). (a): IGS-GIM $(5.6^{\circ} \times 2.8^{\circ})$ with nearest neighbor interpolation; (b): Raw MIT-TEC $(1^{\circ} \times 1^{\circ})$; (c): Masked IGS-GIM $(5.6^{\circ} \times 2.8^{\circ})$; (d): Down-sampled MIT-TEC $(5.6^{\circ} \times 2.8^{\circ})$

preserving image continuity. Chen et al. [35] presented a global and local GAN network based on DCGAN, enhancing the ability to complete arbitrary regions in the image and it achieved good performance even under geomagnetic storms. Later, Pan et al. [36] constructed the SNP-GAN framework, which utilizes a Patch-GAN architecture along with contextual attention and discriminator spectral normalization constraints. SNP-GAN outperforms the previous DCGAN-PB in terms of reconstruction accuracy, recovery rate of ionospheric peak structures, and computational efficiency. It also effectively made completion for large and medium ionosphere structures that were missing in original TEC maps. Yang et al. [37] applied the pix2pixhd model for completing TEC maps, demonstrating a certain level of reliability in completing large-scale missing regions and generating ionospheric peak structures. Its performance was slightly inferior near the edges of the ionospheric peak region.

Moreover, the RFGAN framework was proposed, which was a hybrid deep learning approach combining the dual discriminator conditional GAN (DDcGAN) and Deepfill v2 for free-form image inpainting [38]. It effectively integrated MIT-TEC data, IGS final products, and TEC observations from altimetery satellites, achieving high accuracy performance in both continental and oceanic regions for all geomagnetic conditions.

Those numerous GAN-based framework have been utilized for TEC in-painting tasks. many of these methods employ customized mask shapes and ratios for the input data, restricting the evaluation for inpainting on the original MIT-TEC data.

To address the problem, this work proposed a relatively simple encoder—decoder structure, with only a few hidden layers to achieve better performance and efficient computational costs. The rest of this article is organized as follows. In Section II, data source and methods are introduced. In Section III, the experimental results are described and compared. In Section IV, the discussion is made. Finally, Section V concludes this article.

II. DATA AND METHODS

A. Data Sources

The training data used in this work is the IGS-GIM final products, obtained from the Crustal Dynamics Data and Information System (CDDIS) of the National Aeronautics and Space Administration (NASA) archive. 1 This data have a spatial resolution of 2.5° in latitude and 5° in longitude, with a temporal resolution of 2 hours. To ensure compatibility with the proposed model, nearest neighbor interpolation is employed to resize the data dimensions to 64×64 , facilitating processing within the proposed GAN framework, as illustrated in Fig. 1(a). To conduct the global TEC inpainting, the MIT-TEC is selected as the source data, which can be downloaded from the website. 2 The original size of the MIT-TEC data is 180×360 , as shown in Fig. 1(b). It has a resolution of 1° in both longitude and latitude and a

¹[Online]. Available: ftp://gdc.cddis.eosdis.nasa.gov

²[Online]. Available: http://cedar.openmadrigal.org/

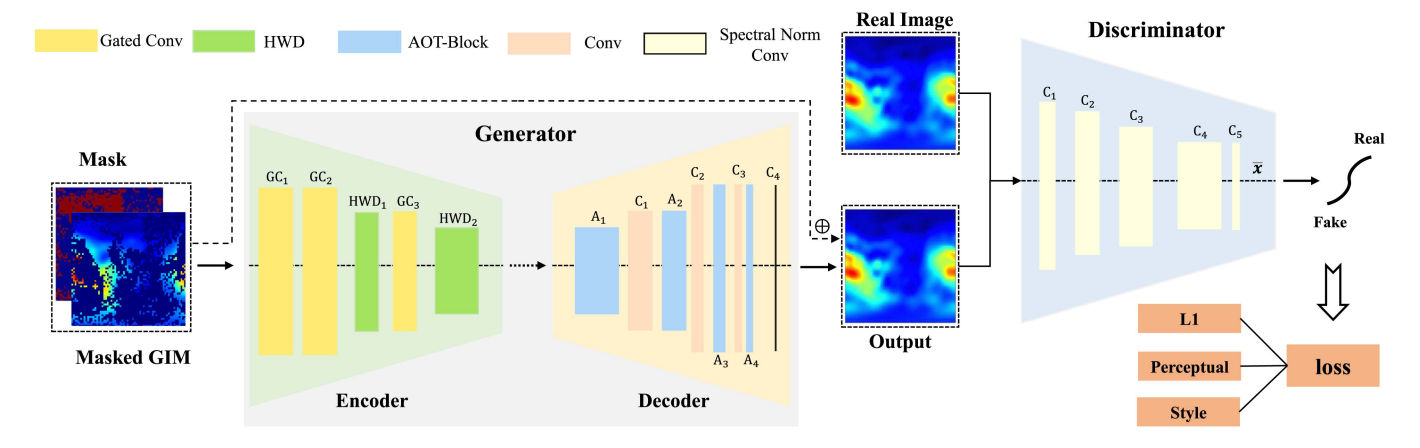


Fig. 2. Generator and discriminator structure of the WTM-GAN model.

temporal interval of 5 min. Despite the high spatial resolution, the spatial coverage is relatively low.

For the in-painting task of MIT-TEC, there are two approaches. The first method, as demonstrated in Fig. 1(c), involves overlaying the MIT mask on IGS-GIM. Initially, the masked IGS-GIM was selected as input for comparison baseline across different GAN-based frameworks. Subsequently, the MIT-TEC image was processed with partially masked ground-truth values, which were then used for performance evaluation. The alternative approach requires direct alignment between MIT-TEC and IGS-GIM, followed by a down-sampling scheme applied to the original MIT-TEC data, resulting in 64×64 grid sizes shown in Fig. 1(d). This down-sampling yields a spatial resolution of 5.625° in latitude and 2.8125° in longitude, while maintaining the original temporal interval of 2 hours. The scheme achieves effective data coverage exceeding 30% for test data, specifically 34.3% in 2014 and 36.1% in 2017 as selected in this work.

For both two ways, the missing regions are indicated by pixel values of zero. It is noted that the two types of data are both normalized in the range of [-1, 1] before the training and testing process.

B. Proposed Framework

The proposed GAN-based framework is composed of encoder–decoder architectures. For the encoder part, a Haar wavelet filter was installed ahead, followed by a transformed down-sampling layers. For the decoder part, a novel segmentation-transformation-merging architecture was proposed, with some parts of module modified from the original AOT-GAN [26]. The proposed wavelet transform and merging generative adversarial network (WTM-GAN), as shown in Fig. 2, has strongly increased the performance of MIT-TEC completion under low resolution situations. To accomplish the proposed in-painting scheme, the following improvements were made.

1) Gated Convolution: Gated convolution was used in the encoder part, instead of the traditional convolution. It is considered as an enhancement to partial convolutions to address the

issue of mask updating [27]. A learnable soft mask updating rule is utilized, expressed as follows:

Gating
$$_{y,x}=\sum\sum W_g\cdot I$$
 (1)

Feature
$$y,x = \sum \sum W_f \cdot I$$
 (2)

$$O_{y,x} = \phi$$
 (Feature $_{y,x}$) $\odot \sigma$ (Gating $_{y,x}$) (3)

where σ is the sigmoid activation function and ϕ is set as the ELU activation function in our experiment. Gated convolution introduces a learnable parameter matrix to distinguish between valid and invalid pixels, and thus has the ability to learn dynamic feature selection for each channel and spatial position, making it very effective in image inpainting tasks.

- 2) Haar Wavelet Transform Down-Sampling (HWD): The Haar wavelet transform is utilized to down-sample the TEC feature maps through a transform-merging approach. Initially, it separates the TEC image into low-frequency and high-frequency signals. From the high-frequency signal, it extracts high-frequency component information in different directions to construct new feature maps [28]. These newly constructed feature maps are then concatenated with the low-frequency signal. Finally, convolution is employed for aggregation, ensuring down-sampling while preserving the maximum possible amount of feature map information.
- 3) Aggregated Contextual Transformation Block (AOT Block): AOT Block employs the segmentation-transformation-merging strategy. Unlike the original paper, where the AOT Blocks are placed after the encoder, we have positioned AOT Blocks with different convolution expansion rates before each upsampling convolution. This enables us to leverage diverse short, medium, and long image context information multiple times across various layers of the decoder for image reconstruction. AOT Block is derived from residual connections, wherein for an input x, the network's layers can map it to F(x). By adding the output x from the previous layer to the output F(x) of the current layer, we obtain H(x), resulting in a residual block. The mathematical expression for this process is as follows:

$$H(x) = F(x) + x. (4)$$

Therefore, the network does not need to learn the identity mapping from x to H(x), it can directly learn the changing part of this identity mapping F(x) = H(x) - x. AOT Block also uses a gating approach on this basis

$$H(X) = g * F(x) + (1 - g) * x$$
(5)

$$g = \sigma \left(k * \left(\frac{2 * (G(x) - \text{mean}(G(x)))}{\text{std}(G(x))} - 1 \right) \right)$$
 (6)

$$G(x) = Gate(x). (7)$$

To obtain the output x, it undergoes two convolutions: one part of the convolution yields G(x) as described in (7), while the other part generates F(x) as depicted in (5). The resulting G(x) is normalized, and the weight g is learned automatically through the sigmoid function. This weight is applied to map F(x), while the remaining part of 1-g is applied to the input x. This connection scheme ensures that the convolution results depend as much as possible on valid pixels, thereby reducing the influence of invalid pixels on the convolution outcomes. Consequently, it preserves the features of the valid pixel region and the learned residual features for aggregation.

4) Loss Functions: Three common loss functions were employed in image inpainting tasks: L_1 Loss, Perceptual Loss, and Adversarial Loss, for loss computation. Each of these loss functions plays a crucial role in the optimization process of our model. L_1 Loss primarily drives the pixel values of the image to closely align with the ground truth. Perceptual Loss enhances the local texture details of the image, while Adversarial Loss determines the stability of model training. The definitions of the three loss functions are as follows. L_1 Loss is defined as

$$L_1 \text{ Loss } = \frac{1}{n} \sum_{i=1}^{n} |y_i - f(x_i)|.$$
 (8)

In the TEC inpainting task, there are 64×64 total 4096 grid points. Perceptual loss is defined as

Perceptual loss =
$$\frac{1}{N} \sum_{i=1}^{N} (F_i(x) - F_i(y))^2$$
 (9)

where $F_i(x)$, $F_i(y)$ represents the layer i feature graph in the pretrained VGG19 network, and N represents the layer number of the feature graph. The Adversarial loss of the generator is

$$L_{\text{adv}}^G = E_{z \sim P_z}[\log(1 - D(G(z)))]. \tag{10}$$

The Adversarial loss of the discriminator is

$$L_{\text{a d v}}^{D} = E_{x \sim P_{\text{data}}}(x) [\log D(x)] + E_{z \sim P_{z}}(z) [\log(1 - D(G(z))]. \tag{11}$$

The above three loss functions are combined into the final loss function, that is

$$Loss = \lambda_1 * L_1 \text{ Loss } + \lambda_2 * \text{ Perceptual Loss } + \lambda_3 * L_{adv}^G$$
(12)

where $\lambda_1, \lambda_2, \lambda_3$ is the weight of each loss.

C. Evaluation Metrics

Three metrics are adopted to evaluate the performance of our proposed framework: root mean square error (RMSE), missing region RMSE (M-RMSE), and peak signal-to-noise ratio (PSNR). RMSE evaluates the performance in accuracy by measuring the average magnitude of the differences between completed values and ground truth. Its mathematical formulation is defined as

RMSE =
$$\sqrt{\frac{\sum_{i=1}^{n} (x_{\text{obs},i} - x_{\text{model},i})^{2}}{n}}$$
. (13)

In this experiment, the variable n represents the total number of TEC grid points. We denote $x_{{\rm obs},i}$ as the predicted value at the ith grid point and $x_{{\rm model},i}$ as the corresponding ground truth value. Equation (13) represents the comprehensive measure of the discrepancy between the estimated values and the ground truth values for all TEC grid points worldwide at a specific time. Considering that the observational data on land are relatively complete, the missing pixels primarily occur in regions such as oceans and polar areas. Therefore, we specifically calculate the RMSE for the missing region to obtain the evaluation metric M-RMSE. This metric has better capability to evaluate the inpainting accuracy for unknown regions, as described in (15)

$$(x_{obs-m,j}, x_{model-m,j}) = \operatorname{select}(x_{obs,i}, x_{model,i})_{i \in (1-\operatorname{mask})}$$
(14)

$$M - RMSE = \sqrt{\frac{\sum_{j=1}^{k} (x_{obs-m,j} - x_{model-m,j})^2}{k}} \quad (15)$$

PSNR is used to assess the quality of inpainting and is closely associated with the mean square error (MSE). It quantifies the ratio between the maximum possible power of a signal and the power of the noise presented in the reconstructed image. The calculation formula for PSNR is given as follows:

MSE =
$$\frac{1}{mn} \sum_{i=0}^{m-1} \sum_{j=0}^{n-1} [I(i,j) - K(i,j)]^2$$
(16)

$$PSNR = 10 \cdot \log_{10} \left(\frac{MAX_I^2}{MSE} \right)$$
 (17)

where I is the reference image IGS-GIM, K is the inpainting image, MAX_I^2 is the maximum pixel value of all points in the image, the unit of PSNR is dB, the higher the PSNR value, the better the reconstruction quality of the image.

III. EXPERIMENTS AND RESULTS

A. Experimental Settings

For this experiment, the MIT-TEC and IGS-GIM datasets spanning from 2018 to 2022 were selected as training data. The validation set comprises data from 2015 and 2016, while the test set encompasses data from 2014 (high solar activity year) and 2017 (low solar activity year). The training process was conducted over 400 epochs, with a single NVIDIA

Period		RMSE↓			M-RMSE↓				PSNR↑				
1 0110 0		Global	Low	Mid	High	Global	Low	Mid	High	Global	Low	Mid	High
	DCGAN	7.527	10.118	6.166	4.327	8.067	10.686	6.634	4.702	21.258	18.723	17.605	16.149
2014	G-CAE	4.724	5.798	4.153	2.912	5.468	6.541	4.608	3.317	25.476	23.737	22.049	19.850
2014	SNP-GAN	3.062	4.054	2.292	2.094	3.174	4.166	2.366	2.156	29.257	26.841	26.548	22.819
	WTM-GAN	2.117	2.764	1.852	1.212	2.326	3.014	1.970	1.323	32.309	30.033	28.154	27.122
2017	DCGAN	4.268	5.576	3.585	2.698	4.623	5.888	3.736	2.948	19.372	17.128	14.663	11.142
	G-CAE	1.647	1.912	1.549	1.025	1.921	2.139	1.719	1.183	27.905	26.691	23.013	20.352
	SNP-GAN	1.692	2.279	1.335	0.944	1.799	2.539	1.208	0.897	27.719	25.179	23.731	21.097
	WTM -GAN	0.908	1.175	0.818	0.516	1.011	1.281	0.876	0.578	32.931	30.753	27.528	25.850
	DCGAN	8.511	11.401	7.075	4.901	9.102	11.961	7.546	5.262	20.907	18.379	17.486	16.704
Storm A	G-CAE	5.688	6.816	5.010	3.758	6.568	7.623	5.462	4.329	24.504	22.990	21.799	19.058
Storm A	SNP-GAN	3.164	4.250	2.136	2.293	3.290	4.351	2.185	2.380	29.717	27.147	28.096	23.862
	WTM -GAN	2.315	2.989	2.091	1.288	2.537	3.220	2.182	1.421	32.217	30.028	28.182	28.257
C4 D	DCGAN	4.749	6.455	3.931	2.563	5.141	6.869	4.178	2.852	20.869	18.247	15.803	13.389
	G-CAE	1.767	2.235	1.483	1.141	2.137	2.630	1.732	1.352	29.552	27.562	25.085	20.584
Storm B	SNP-GAN	1.802	2.548	1.329	0.913	2.256	3.159	1.695	1.116	30.653	27.752	26.413	23.747
	WTM -GAN	1.196	1.554	1.004	0.794	1.343	1.732	1.096	0.886	32.963	30.685	27.862	23.784

TABLE I
ERROR STATISTICS OF THE MODEL COMPLETING DIFFERENT REGIONS IN DIFFERENT TIME PERIODS

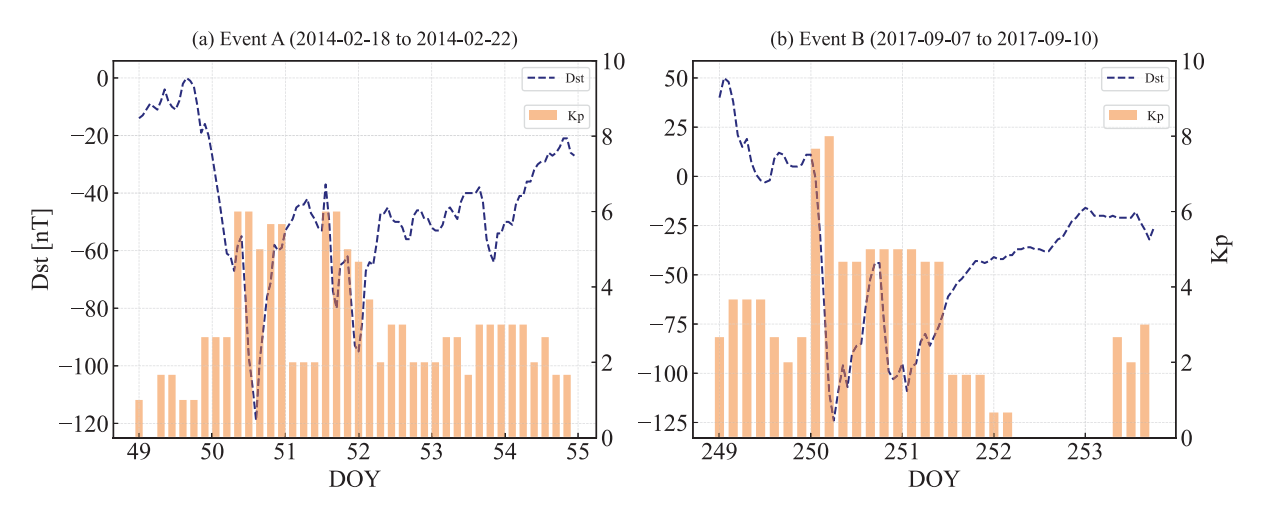


Fig. 3. Dst index and Kp index during the two geomagnetic storms. (a) Storm A in 2014 and (b) storm B in 2017.

Tesla V100 GPU. In average, a complete training session took approximately 8 hours. To ensure optimal performance, the model hyperparameters were extensively tuned.

In the proposed framework, both the generator and discriminator were optimized using the Adam optimizer, with a learning rate of 1e-4, beta1=0.5, and beta2=0.999. The weights assigned to the loss functions were set as follows: $\lambda_1=1, \lambda_2=0.1, \lambda_3=0.05$. The batch size was set to 64. Within each AOT-Block, the dilation rates of the convolutional layers in the different branches were set to 1, 2, 4, and 8, respectively. The above hyperparameters are finally determined by the optimization method of grid search.

B. Performance of Models

The WTM-GAN was compared with several representative generative frameworks, such as deep convolutional generative adversarial network (DCGAN), gated convolutional autoencoder (G-CAE), and spectral normalization patch-based generative adversarial network (SNP-GAN). The comparison results are shown in Table I.

To evaluate the generalization ability of our model WTM-GAN, RMSE, M-RMSE, and PSNR for different regions were computed in the test dataset. Specifically, the global regions were separated into three parts for evaluation, low-latitude (-30° to 30°), midlatitude (-60° to -30° and 30° to 60°), and highlatitude (-90° to -60° and 60° to 90°). Both the yearly and the geomagnetic disturbance periods test datasets were considered for experiments.

The Kp and Dst indices [39] were utilized to identify periods of geomagnetic storms. As illustrated in Fig. 3, the dashed blue line in panels (a) and (b) represents the Dst index, while the orange bar denotes the Kp index. Two representative geomagnetic

storms were selected for analysis: Storm A, spanning 18–22 February 2014, and Storm B, occurring from 7 to 10 September 2017. Both storms exhibited a minimum Dst index below –100 nT, classified as strong storms.

The results presented in Table I clearly indicate that the WTM-GAN framework outperforms the alternative generative models in terms of inpainting errors for the same test dataset. For the entire year of 2014, the solar maximum year in SC24, the RMSE and PSNR values all achieved lowest level in the statistical results, which are recorded as 2.117 TECu and 32.309 dB, respectively. Similarly, for the entire year of 2017, the RMSE and PSNR values are 0.908 TECu and 32.931 dB, respectively. Notably, these values are significantly lower than those computed by DCGAN, G-CAE, and SNP-GAN, highlighting the superior performance of the proposed framework. Regarding the M-RMSE metric, which specifically focuses on the error in the missing regions, it is noticed that models can only rely on limited information from the surrounding pixels since there is no ground truth mapping available for these regions. Consequently, the error tends to increase to a certain extent. In regions with larger missing areas and notable TEC variations, such as the EIA region, the error tends to further escalate. However, owing to the distinctive network architecture of WTM-GAN, the model exhibits exceptional capability in extracting valuable information from the valid regions of the image and inferring the missing regions more accurately. Thus, the M-RMSE values for 2014 and 2017 are only 2.326 TECu and 1.011 TECu, respectively. These results manifest the lowest test errors among the compared models, with an increase of merely 0.209 TECu and 0.103 TECu,

During the two geomagnetic storms, the performance of WTM-GAN remains superior. In Storm A, the test errors in the low-latitude, midlatitude, high-latitude, and global average regions are slightly higher compared to the entire year of 2014. However, WTM-GAN still achieves remarkable performance, with a global RMSE, M-RMSE, and PSNR of 2.315 TECu, 2.537 TECu, and 32.217 dB, respectively. These values are significantly lower than those obtained by the other models. Similarly, in Storm B, WTM-GAN exhibits a global RMSE, M-RMSE, and PSNR of 1.196 TECu, 1.343 TECu, and 32.963 dB, respectively, indicating a slight increase in errors compared to the entire year. For different latitudes, it is observed that the low-latitude region experiences larger errors compared to the midlatitude and high-latitude regions. This discrepancy can primarily be attributed to the presence of the equatorial ionization anomaly, characterized by higher TEC values and more significant TEC variations. This region is prone to abnormal TEC values that exceed the normal range. Consequently, when completing in the vicinity of this region, the model tends to underestimate the TEC variation features, only aligning it with the normal TEC features. In contrast, the midlatitude and highlatitude regions generally exhibit lower TEC values and normal cyclic variations, with less response to geomagnetic storms. Therefore, completing in these regions can follow their expected trends. Additionally, it is important to consider the nonuniform distribution of the MIT mask across different latitudes and longitudes, reflecting the distribution pattern of stations located

on land and certain islands. The low-latitude region has less reference data available, while the midlatitude regions, with more land coverage, possess a greater number of reference data and more reliable information from the adjacent pixels. As a result, the completing reliability in these regions is higher.

Fig. 4 presents the inpainting results of multiple frameworks at four specific time points during a geomagnetic quiet period from 00:00 to 06:00 UT on 1 January 2017. The first column depicts the masked GIM data requiring inpainting, while the last column displays IGS-GIM. These inpainting results demonstrate that WTM-GAN consistently achieves the highest level of inpainting accuracy and preserves image continuity, closely resembling the inpainting process of IGS-GIM. Notably, WTM-GAN exhibits minimal errors in reconstructing the overall TEC contours and capturing fine structures in regions that exhibit extreme values. To provide a more intuitive evaluation of the inpainting accuracy and the challenges encountered by each model in different regions, the errors of individual pixels within the TEC maps were further analyzed throughout the entire test datasets or during the periods of geomagnetic storms.

During periods of geomagnetic storms characterized by significant TEC variations, the inpainting results of each framework was presented at the stages of storm occurrence in Figs. 5 and 6. Fig. 5 showcases the results during the occurrence of storm A on 18 February 2014, from 20:00 to 22:00 UT, while Fig. 6 displays the results during the occurrence of storm B on 8 September 2017, from 14:00 to 16:00 UT. the masked GIM data were input into each framework to obtain the corresponding inpainting results: these four frameworks considered were DCGAN, G-CAE, SNPGAN, and WTM-GAN. Results are then compared with the IGS-GIM ground truth data. The inpainting results clearly demonstrate that WTM-GAN excels in recovering a more comprehensive TEC structure compared to the other models, particularly in capturing the equatorial ionospheric dual-peak structure during the geomagnetic storms. SNP-GAN and G-CAE also exhibit relatively good performance during storm A and storm B, respectively. For the Global RMSE, it consistently reveals that WTM-GAN achieves the lowest RMSE values during the periods of geomagnetic storms. Specifically, at 20:00 and 22:00 UT, the RMSE values are computed as 2.726 TECu and 2.443 TECu, respectively, slightly higher than the annual values of 2.117 TECu in 2014. During storm B, at 14:00 and 16:00 UT, the RMSE values are 1.409 TECu and 1.543 TECu, respectively, slightly higher than the annual values of 0.908 TECu in 2017. Notably, the increase in RMSE remains within 0.65 TECu, demonstrating the consistent and reliable inpainting capability of WTM-GAN under various geomagnetic conditions.

Fig. 7 illustrates the global distribution of RMSE for four effective inpainting models. Fig. 7(a), (c), (e), and (g) shows the annual mean RMSE values for 2014, while Fig. 7(b), (d), (f), and (h) depicts the annual mean RMSE values for 2017. Fig. 7 reveal that in 2014, the models exhibit relatively large errors. For instance, in 7(a) and (c), DCGAN and G-CAE display a significant portion of RMSE values around 10 TECu in the midlatitude and low-latitude regions, as indicated by the red areas. Similarly, in Fig. 7(e), SNP-GAN shows areas with substantial errors in the

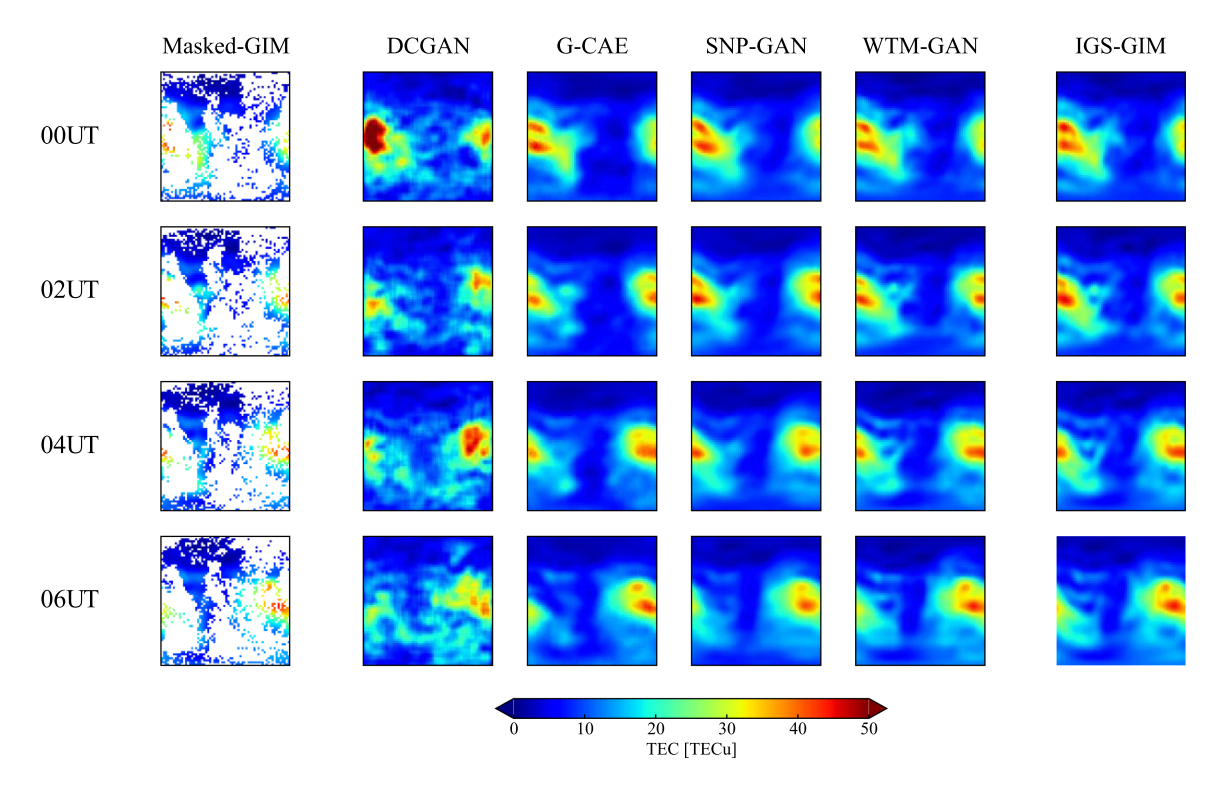


Fig. 4. Model inpainting results in 1 January 2017 00:00-06:00UT (Quiet period).

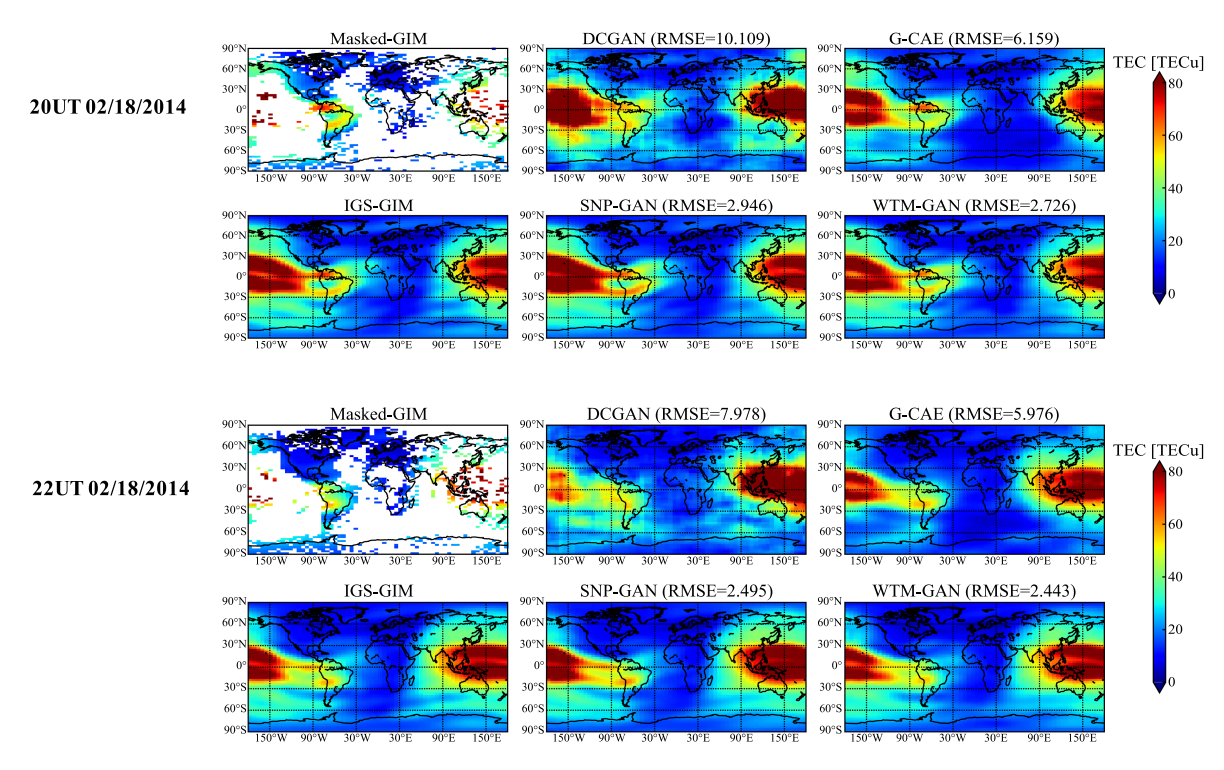


Fig. 5. Inpainting results during geomagnetic Storm A (18–22 February 2014).

low-latitude region. However, compared to G-CAE, SNP-GAN successfully reduces the errors. In Fig. 7(g), WTM-GAN further decreases the inpainting errors in the low-latitude region, with the majority of the inpainting areas exhibiting RMSE values below 6 TECu, and a considerable portion achieving RMSE

values below 4 TECu. In 2017, owing to lower solar activity levels and stable TEC variations, the inpainting errors of the models in the low-latitude region are generally reduced by approximately 3-6 TECu compared to 2014. However, Fig. 7(d) and 7(f) still indicates some regions with relatively large errors

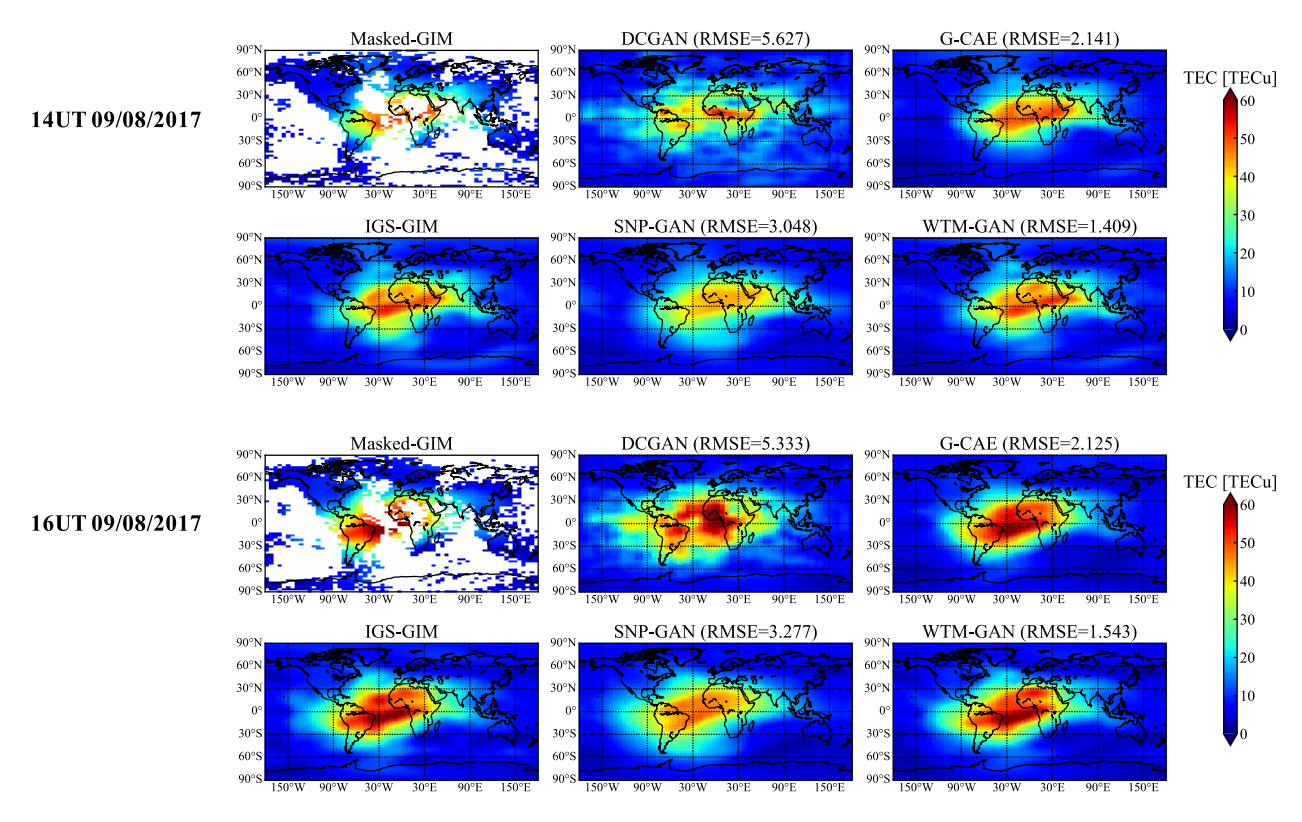


Fig. 6. Inpainting results during geomagnetic Storm B (7–10 September 2017).

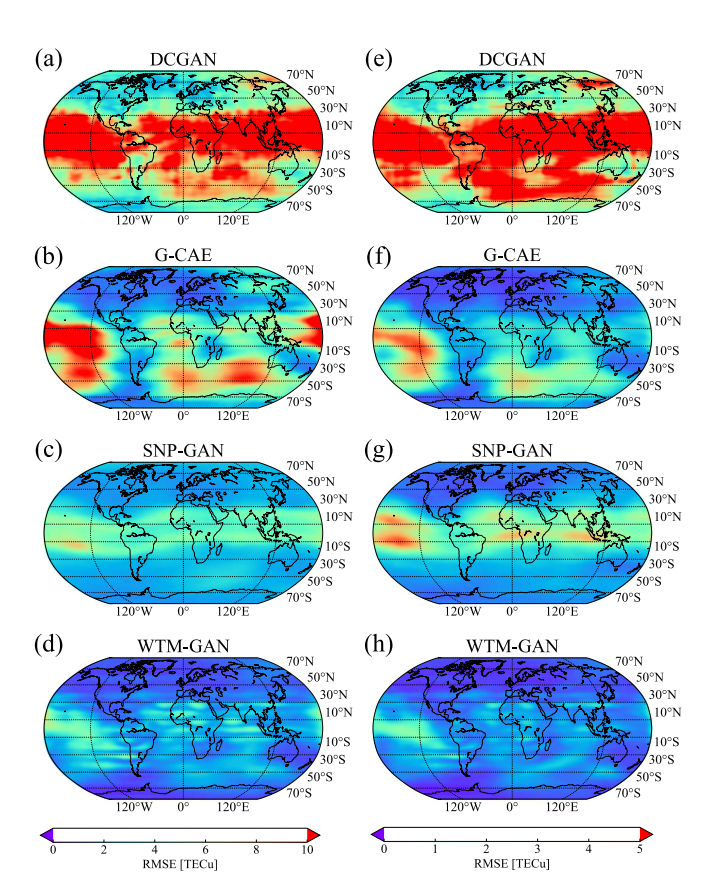


Fig. 7. Global RMSE distribution of each model. (a)–(d) in 2014 and (e)–(h) in 2017.

in the low-latitude region. In contrast, Fig. 7(h) demonstrates the inpainting results of WTM-GAN, which consistently exhibit low errors in a global scale, demonstrating the excellent TEC inpainting capability during both the solar maximum and solar descending years.

A statistical analysis of RMSE was conducted for those four GAN-based frameworks based on the test datasets. The results are presented in the RMSE occurrence distribution histograms shown in Fig. 8. Fig. 8(a) and (b) shows the results for 2014 and 2017, respectively, while Fig. 8(c) and (d) displays the results for Storm A and Storm B. The x-axis of all subplots represents the RMSE values, while the y-axis represents the occurrence values. Regarding the RMSE distribution, the inpainting results of WTM-GAN consistently reveal a left-skewed distribution in every tested time period, indicating fewer outliers. To assess the error reduction capability of WTM-GAN, we calculated the proportions of RMSE distributions below 5 TECu for 2014 and Storm A, as well as the proportions below 2 TECu for 2017 and Storm B, as shown in Table II. WTM-GAN achieves a proportion of RMSE distributions below 5 TECu of 99.12% for 2014 and 98.46% for Storm A, which is significantly higher compared to G-CAE and SNP-GAN. In the low solar activity year of 2017, WTM-GAN achieves an impressive proportion of RMSE distributions below 2 TECu of 97.90%, demonstrating its stability in inpainting during periods of low solar activity. In the case of Storm B, the proportion of RMSE distributions below 2 TECu slightly decreases for WTM-GAN but still reaches 94.31%.

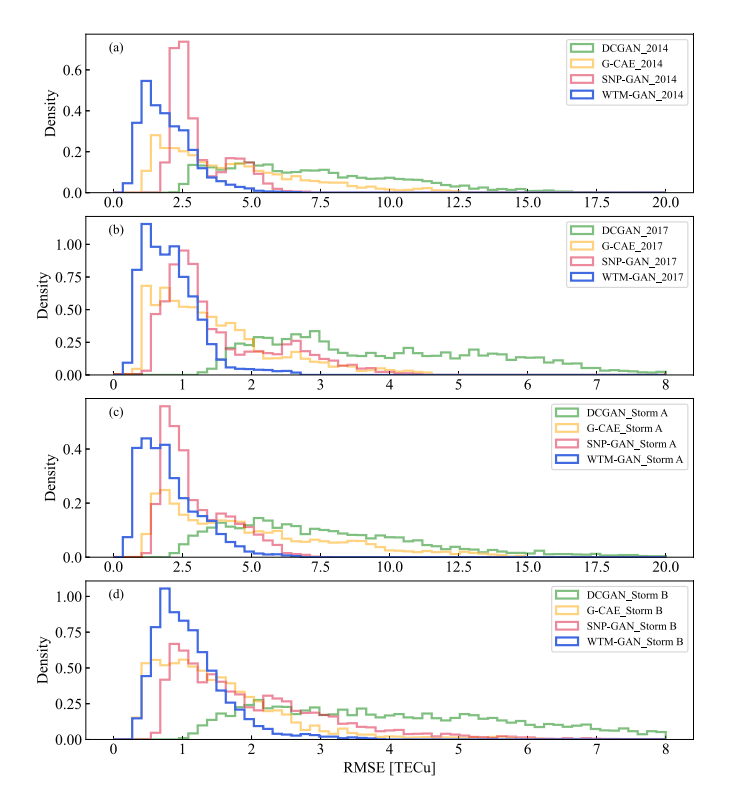


Fig. 8. Histogram of global RMSE frequency distribution for each model.

TABLE II PERCENTAGE OF MODEL ERRORS WITHIN ACCEPTABLE THRESHOLDS: <5 TECU for 2014 and <2 TECU for 2017

	P(RMSE	C<5TECu)	P(RMSE<2TECu)		
Models	2014	Storm A	2017	Storm B	
DCGAN	32.51%	27.57%	11.70%	14.91%	
G-CAE	68.51%	61.18%	79.39%	77.49%	
SNP-GAN	94.09%	92.24%	72.39%	64.50%	
WTM-GAN	99.12%	98.46%	97.90%	94.31%	

C. Single Point Error Statistics At Different Locations

To assess the accuracy of the models in inpainting at different latitudes (as longitude has a lesser impact on inpainting errors compared to latitude, it is not extensively discussed), quantitative evaluations using RMSE and PSNR were conducted at selected locations. In the selection, each three points in low, middle, and high latitudes in MIT-TEC data coverage were considered, together with each three points at the same region without MIT-TEC data coverage.

The geographical coordinates of these selected points are provided in Table III. The first two rows represent the chosen points within areas covered by MIT-TEC observation data, while the third and fourth rows represent the points in regions where MIT-TEC data was missing. The spatial distribution of the selected points and the statistical analysis of their RMSE

and PSNR values are presented in Fig. 9. It is noticed that for the selected points shown in Fig. 9(c), their RMSE values are equivalent to the M-RMSE metric defined in Section III. As they are located in regions without MIT-TEC data coverage. During the calculation process, taking into account the limited grid resolution (5.625° in longitude and 2.8125° in latitude), the selected points were assigned to the corresponding grid points and the grid point errors were considered as the errors for those points.

In Fig. 9(b) and (d), the subplots labeled as (I), (II), (III), and (IV) represent the statistical results for 2014, Storm A, 2017, and Storm B, respectively. The bar charts illustrate the RMSE values, while the line charts depict the PSNR values. The findings demonstrate that RMSE levels within the same latitude range are relatively consistent, displaying a pattern of slightly larger errors at low latitudes and smaller errors at mid-to-high latitudes. Moreover, low latitude points are more susceptible to the impact of storms, resulting in increased errors. In contrast, mid-to-high latitude points, especially those at high latitudes, are less affected by storms and exhibit relatively stable errors during storm periods. The comparative analysis of the three frameworks reveals that WTM-GAN consistently maintains the lowest errors across all selected points and exhibits the smallest increment in errors during storm periods. This indicates that WTM-GAN possesses stable inpainting capabilities even during geomagnetic storm periods, surpassing the performance of the G-CAE and SNP-GAN models. When the selected points are situated in regions without MIT-TEC data coverage, there is a slight increment in test errors. This is attributed to the fact that the land regions in the inpainting process utilize the ground truth as the background condition, while the missing regions need to learn the mapping of the network. However, the proposed framework has significantly reduced this error and preserved the available ground truth data as much as possible, resulting in a low overall average error level.

Finally, the daily average PSNR on the test dataset was computed and presented in Fig. 10. Fig. 10(a) and (b) displays the statistical outcomes for 2014 and 2017, respectively. It shows that WTM-GAN consistently achieves the highest PSNR values throughout the entire year on the test datasets. In both Fig. 10(a) and (b), the PSNR values for WTM-GAN are predominantly above 30 dB. Furthermore, when compared to SNP-GAN and G-CAE, WTMGAN exhibits smaller fluctuations in PSNR values, indicating a more stable quality of image reconstruction. The inpainting outcomes for the masked GIM unequivocally demonstrate that our framework surpasses others in terms of inpainting quality and stability.

D. Completion of MIT-TEC

In practical applications, since there already exists a complete IGS-GIM dataset as a reference, the main purpose of completing the Masked GIM, as mentioned earlier, is to validate the effectiveness of GANs in inpainting. The inpainting results serve as a reference solely for comparing the performance of different frameworks. However, the MIT-TEC dataset, which represents the actual observation values from land-based

TABLE III

LATITUDE-LONGITUDE DISTRIBUTION OF SELECTED MIT-TEC MEASUREMENT POINTS: LAND LOCATIONS (TOP ROW) AND OCEAN/POLAR REGIONS (BOTTOM ROW)

	Low1	Low2	Low3	Mid1	Mid2	Mid3	High1	High2	High3
Lat	0	25	-12.5	37.5	-50	40	62.5	80	-75
Lon	30	115	-40	135	-70	-90	-160	25	-120
Lat	0	25	-12.5	37.5	-50	-40	62.5	80	-75
Lon	-120	-30	80	160	0	120	100	-140	60

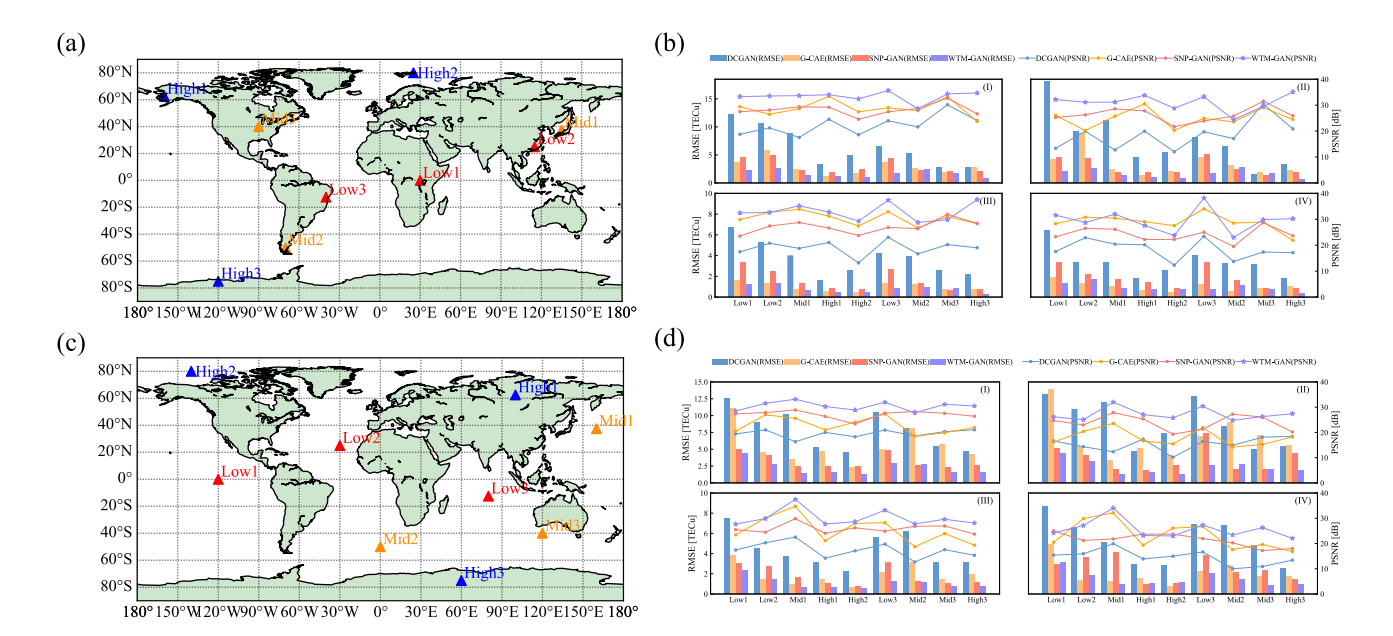


Fig. 9. Spatial distribution and error calculation results. (a) and (b) Land points and errors. (c) and (d) Ocean/polar points and errors.

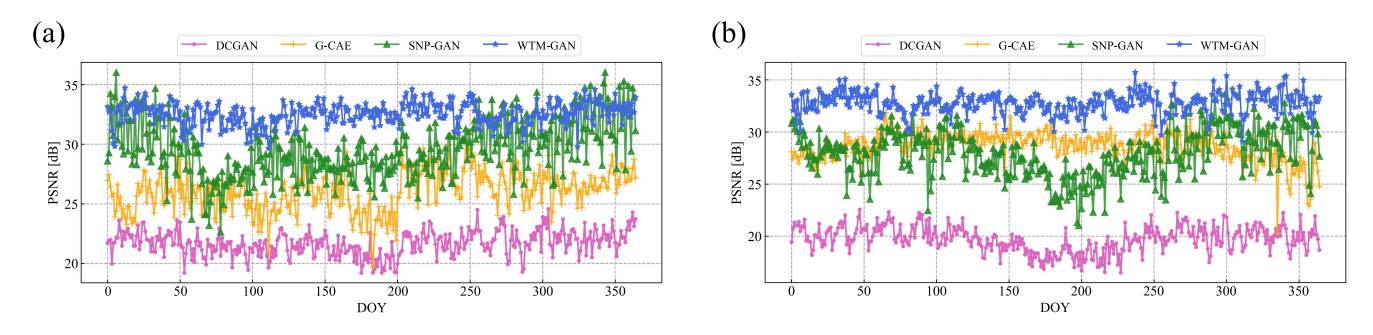


Fig. 10. Daily average value of PSNR for each model (a) 2014. (b) 2017.

stations, holds greater importance as the primary reference. The ultimate objective in this work is to effectively complete the MIT-TEC dataset with the proposed GAN-based framework. Having obtained a trained WTM-GAN inpainting model for the Masked GIM inpainting task, the model mentioned in Section III is used as a pretrained model for MIT-TEC inpainting. It is reasonable since MIT-TEC exhibits a similar data distribution to the Masked GIM, as shown in Fig. 11 (where zero-free distributions represent original data, while zero-included distributions show MIT-TEC with missing values filled as zeros). With a "pretraining and fine-tuning" learning

strategy shown in Fig. 12, the proposed model can be further proceeded to accomplish the MIT-TEC inpainting task.

For the reference data required during the transfer learning training, a fusion method was employed that combines MIT-TEC with IGS-GIM. The proposed fusion method involves incorporating the MIT-TEC values in observed areas such as land into the IGS-GIM values in data vacancy areas such as oceans and polar regions. The fused image is obtained through bilateral filtering [40], which not only preserves the ground truth of MIT-TEC but also retains some gradient information from the MIT-TEC images.

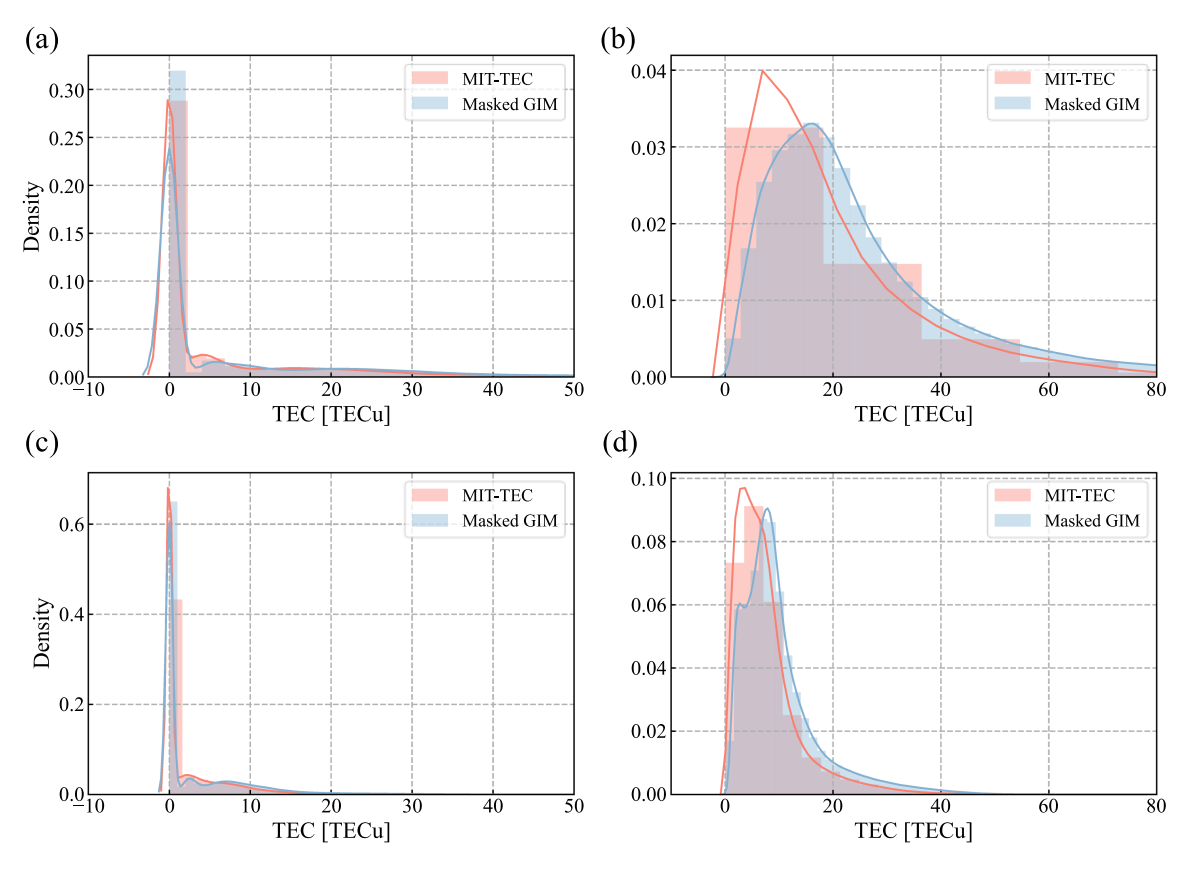


Fig. 11. Data distribution of MIT-TEC and Masked GIM. (a) and (b) 2014 with/without zeros. (c) and (d) 2017 with/without zeros.

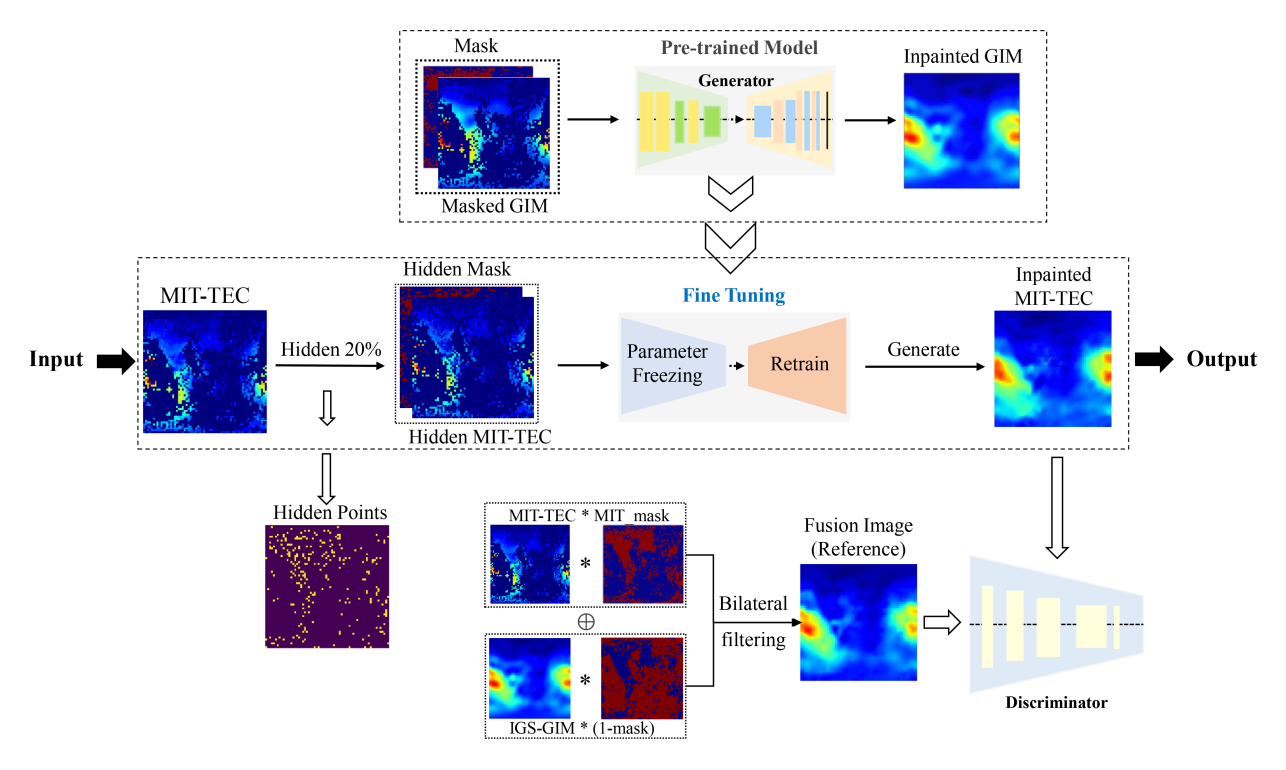


Fig. 12. Flowchart of MIT-TEC Inpainting via preptraining and Fine-tuning: Model training with MIT-TEC/GIM fusion and 20% masked-point evaluation.

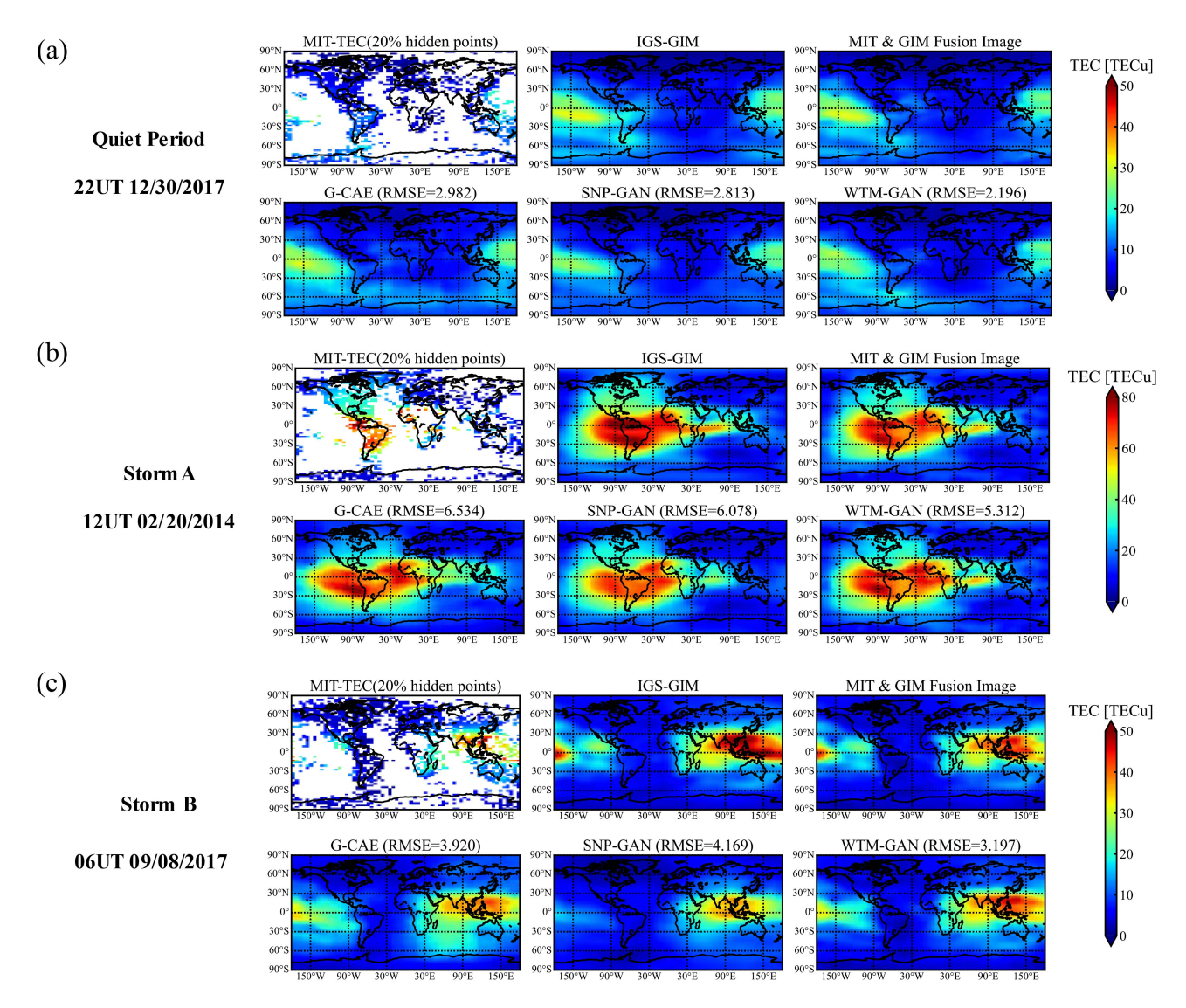


Fig. 13. MIT-TEC inpainting results during quiet period and storm. (a): results at 22 UT December 30, 2017 (Quiet Period); (b): results at 12 UT February 20, 2014 (Storm A); and (c): results at 06 UT September 8, 2017 (Storm B).

The results of MIT-TEC completion using the fine-tuned WTM-GAN model are presented in Fig. 13. It shows the inpainting outcomes during one quiet period and two storm periods, then compares them with the MIT-TEC inpainting results obtained from other models. The RMSE values indicated in the title of each subplot represent the RMSE calculated specifically for the 20% hidden points, rather than the error of the entire image. It is worth noticing that the error of the entire image is significantly lower than the RMSE calculated by 20% hidden points. The inpainting results clearly demonstrate that WTM-GAN achieves the lowest inpainting errors. It is capable of reconstructing ionospheric maps with minimal errors not only during geomagnetic quiet periods but also during geomagnetic storm periods. Furthermore, during geomagnetic storm periods, WTM-GAN exhibits the greatest ability to reconstruct the equatorial dual-peak structure of the ionosphere, as depicted in Fig. 13(b) and (c).

Similarly, the RMSE and PSNR for the entire year and geomagnetic storm periods were computed, as shown in Table IV. The results indicate that WTM-GAN demonstrates superior inpainting performance. The RMSE values for 2014 and 2017 are 7.075 TECu and 2.604 TECu, respectively, which fall within a reasonable range. During Storm A and Storm B, the RMSE values are 5.661 TECu and 3.143 TECu, respectively. WTM-GAN consistently achieves PSNR values greater than 30 dB in all events, indicating a high quality of reconstruction for MIT-TEC images. In contrast, the PSNR values of the other comparative models all fall below 30 dB. Consequently, WTM-GAN can be regarded as a new framework for effectively inpainting TEC maps, with improved inpainting performance.

IV. DISCUSSION

The above experiments verified the completion capability for WTM-GAN with data from different solar phases (2014 and

Period		RMSE	PSNR
	DCGAN	11.345	24.447
2014	G-CAE	10.104	25.786
2014	SNP-GAN	8.052	27.884
	WTM-GAN	7.075	30.287
	DCGAN	6.182	25.266
2017	G-CAE	3.315	29.637
2017	SNP-GAN	3.130	29.242
	WTM-GAN	2.604	32.007
	DCGAN	10.501	24.099
C4 A	G-CAE	7.286	27.372
Storm A	SNP-GAN	6.242	29.123
	WTM-GAN	5.661	30.299

TABLE IV
ERROR STATISTICS OF MODELS INPAINTING MIT-TEC IN DIFFERENT TIME
PERIODS

8.218

3.838

3.991

3.143

23.625

28.918

27.597

31,092

DCGAN

G-CAE

SNP-GAN

WTM-GAN

Storm B

2017) and different geomagnetic storm events (the February 2014 and September 2017 geomagnetic storms) [41], [42]. The performance of WTM-GAN was compared with three GAN frameworks: DCGAN, G-CAE, and SNP-GAN.

TEC data completion with large vacancy ratios always poses challenge for those traditional GAN-based frameworks, leading to unsatisfactory performances. To solve the problem, WTM-GAN adopts a more flexible modeling scheme, in face of some defects hidden in traditional frameworks: for instance, to treat all the pixels equally despite the lack of observations; to employ a gated mask for improvement of model accuracy but with imperfect network constructions, too simple network or too complicated network.

With only a small number of additional hidden layers, the proposed WTM-GAN framework rightly leverages the computational burdens. With gated convolution and Haar wavelet transformation, those defined effective pixels can be easily distinguished from the mask, preserving as much feature map information as possible. The segmentation-aggregationtransformation strategy of the AOT Block makes sure the decoding process with global multiscale information for effective image reconstruction [26]. Therefore, the overall structure of WTM-GAN has more effective feature extraction and restoration capabilities. The experimental results show that the TEC inpainting framework based on the WTM-GAN model archives better completion capabilities compared to other traditional GAN models. The WTM-GAN model has a relatively compact structure and a shorter training time. Most importantly, it can easily keep balance between completion accuracy and computational complexity. In the ablation experiments, as shown in Table V, it should be noted that "1" represents the model with only the addition of AOT-Block, and "2" represents the model with the addition of both AOT-Block and HWD. The table

data demonstrates the different contributions of each module in the WTM-GAN model for better performance, indicating the necessity for all modules in the WTM-GAN framework.

The performance stability of WTM-GAN has been validated during different geomagnetic conditions, showing the strong robustness of this framework in completion of real MIT-TEC data. For further validation, two types of input data are considered in the experiments, one type is IGS-GIM with MIT mask, the other is directly MIT-TEC. It shows that WTM-GAN achieves the best performance in terms of multiple evaluation metrics. This should be attributed to the fact that the construction of WTM-GAN usefully learns the advantages and defects of other GAN-based frameworks. The original goal of the task is to complete the MIT-TEC to get a combined and refined global TEC morphology.

Despite the satisfied performance of the current WTM-GAN framework, there still remains a problem to be noticed. The performance of this framework is influenced by the extensive missing data of TEC in middle-to-low latitudes as well as the unpredictable occurrence of geomagnetic storms. Although the network in WTM-GAN has learned various TEC fluctuation patterns during both geomagnetic quiet and disturbed periods, it may still underestimate the unexpected patterns. In future work, the underestimation of the network during geomagnetic storms will be focused on, and a possible solution is to introduce physical information with parameters, such as the solar activity indices and geomagnetic indices, meanwhile to fully consider the coupling mechanisms in the space physical nature of the ionosphere [43]. With a physics-informed strategy, the problem mentioned above may be well and even completely solved.

V. CONCLUSION

In this work, a novel ionospheric TEC spatial inpainting framework, namely WTM-GAN, is proposed and evaluated. WTM-GAN utilizes an encoder with gated convolutions and Haar wavelet down-sampling, and a decoder with layer-wise segmentation, transformation, and merging. The new framework achieves efficient performance in image restoration.

RMSE, M-RMSE, and PSNR were used to evaluate the inpainting results. Through comprehensive experiments, WTM-GAN demonstrates outstanding inpainting performance in latitudes regions, during both geomagnetic quiet and disturbed periods. It consistently achieves the lowest error values among several comparative models in multiple error metrics, and it successfully captured the features and reproduced the equatorial anomaly dual-peak structure in the ionosphere during geomagnetic storms.

Moreover, the test errors for different latitude positions were calculated with varying degrees of MIT mask coverage and missing regions. The results consistently indicate that WTM-GAN outperforms other comparative models. Even when inpainting MIT-TEC images with 20% hidden points, our model still achieves the lowest error, highlighting its stable inpainting performance for diverse input data, showing the potential applicability of WTM-GAN in more practical scenarios.

TABLE V								
ABLATION EXPERIMENT OF THE WTM-GAN MODEL								

Model	AOT Block	HWD	Gated Conv _	RMSE↓		MAE↓		PSNR↑	
				2014	2017	2014	2017	2014	2017
1	*			2.381	1.073	1.686	0.777	31.301	31.577
2	*	*		2.338	1.008	1.641	0.707	31.413	31.999
WTM-GAN	*	*	*	2.117	0.908	1.491	0.644	32.309	32.931

REFERENCES

- X. Ji, J. Li, and Q. Yang, "Annual characteristic analysis of ionosphere reflection from middle-latitude HF over-the-horizon radar in the northern hemisphere," *IEEE Trans. Geosci. Remote Sens.*, vol. 61, 2023, Art. no. 5104117.
- [2] X. Yue, W. S. Schreiner, Y. Kuo, J. Braun, Y. Lin, and W. Wan, "Observing system simulation experiment study on imaging the ionosphere by assimilating observations from ground GNSS, LEO-Based radio occultation and ocean reflection, and cross link," *IEEE Trans. Geosci. Remote Sens.*, vol. 52, no. 7, pp. 3759–3773, Jul. 2014.
- [3] K. Durga Reddybattula and S. Kumar Panda, "Performance analysis of quiet and disturbed time ionospheric TEC responses from GPSbased observations, IGS-GIM, IRI-2016 and SPIM/IRI-Plas 2017 models over the low latitude Indian region," *Adv. Space Res.*, vol. 64, no. 10, pp. 2026–2045, Nov. 2019.
- [4] P. M. Kintner and B. M. Ledvina, "The ionosphere, radio navigation, and global navigation satellite systems," Adv. Space Res., vol. 35, no. 5, pp. 788–811, Jan. 2005.
- [5] T. P. Yunck, "Coping with the atmosphere and ionosphere in precise satellite and ground positioning," *Geophys. Monograph Ser.*, vol. 73, pp. 1–16, 1993.
- [6] S. Jin, E. Cardellach, and F. Xie, GNSS Remote Sensing Theory, Methods and Applications. Berlin, Germany: Springer, 2014.
- [7] L. Li and S. Jin, "Ionospheric behaviors and characteristics in Asian sector during the Apr. 2023 geomagnetic storm with multi-instruments observations," *J. Atmospheric Sol.- Terr. Phys.*, vol. 259, pp. 106238–106238, Apr. 2024.
- [8] M. Ma, S. Jin, and X. T. Jin, "Characteristics of ionospheric disturbances during the 2021 typhoon Chanthu based on GPS and GLONASS," in *Proc.* Adv. Space Res., 2024, vol. 74, no. 1, pp. 271–283.
- [9] S. Jin, G. P. Feng, and S. Gleason, "Remote sensing using GNSS signals: Current status and future directions," *Adv. Space Res.*, vol. 47, no. 10, pp. 1645–1653, May 2011.
- [10] A. Rovira-Garcia, Deimos Ibáñez Segura, R. Orus-Perez, M. Juan, J. Sanz, and G. González-Casado, "Assessing the quality of ionospheric models through GNSS positioning error: Methodology and results," GPS Solutions, vol. 24, no. 1, 2020.
- [11] M. Juan, J. Sanz, and G. González-Casado, "A worldwide ionospheric model for fast precise point positioning," *IEEE Trans. Geosci. Remote Sens.*, vol. 53, no. 8, pp. 4596–4604, Aug. 2015.
- [12] W. Rideout and A. Coster, "Automated GPS processing for global total electron content data," GPS Solutions, vol. 10, no. 3, pp. 219–228, May. 2006.
- [13] J. Vierinen, A. J. Coster, W. C. Rideout, P. J. Erickson, and J. Norberg, "Statistical framework for estimating GNSS bias," *Atmospheric Meas. Techn.*, vol. 9, no. 3, pp. 1303–1312, Mar. 2016.
- [14] A. J. Mannucci, B. D. Wilson, D. N. Yuan, C. H. Ho, U. J. Lindqwister, and T. F. Runge, "A global mapping technique for GPS-derived ionospheric total electron content measurements," *Radio Sci.*, vol. 33, no. 3, pp. 565–582, May 1998.
- [15] X. Ren, H. Liu, J. Zhang, D. Mei, and X. Zhang, "An improved method for ionospheric TEC estimation using the spaceborne GNSS-R observations," *IEEE Trans. Geosci. Remote Sens.*, vol. 60, 2022, Art. no. 5803812.
- [16] D. Bilitza, "IRI the international standard for the ionosphere," Adv. Radio Sci., vol. 16, pp. 1–11, Sep. 2018.
- [17] P. Chen, W. Yao, and X. Zhu, "Combination of ground- and space-based data to establish a global ionospheric grid model," *IEEE Trans. Geosci. Remote Sens.*, vol. 53, no. 2, pp. 1073–1081, Feb. 2015.
- [18] H. Marew, A. Agmas, and T. Mersha, "Performance evaluation for vertical TEC predictions over the east africa and south America: IRI-2016 and IRI-2020 versions," Adv. Space Res., vol. 73, no. 1, pp. 698–715, Jan. 2024.

- [19] L. Liu, Y. Jade Morton, Y. Wang, and K.-B. Wu, "Arctic TEC mapping using integrated LEO-Based GNSS-R and ground-based GNSS observations: A simulation study," *IEEE Trans. Geosci. Remote Sens.*, vol. 60, 2022, Art. no. 5802410.
- [20] X. Ren, J. Chen, X. Li, X. Zhang, and M. Freeshah, "Performance evaluation of real-time global ionospheric maps provided by different IGS analysis centers," GPS Solutions, vol. 23, no. 4, Aug. 2019, Art. no. 113.
- [21] M. Hernández-Pajares et al., "The IGS VTEC maps: A reliable source of ionospheric information since 1998," *J. Geodesy*, vol. 83, no. 3–4, pp. 263–275, Feb. 2009.
- [22] Q. Zhang, Y. Yao, J. Kong, X. Ma, and H. Zhu, "A new GNSS TEC neural network prediction algorithm with the data fusion of physical observation," *IEEE Trans. Geosci. Remote Sens.*, vol. 61, 2023, Art. no. 5801612.
- [23] J. Feng, T. Zhang, W. Li, Z. Zhao, B. Han, and K. Wang, "A new global TEC empirical model based on fusing multi-source data," GPS Solutions, vol. 27, no. 1, Nov. 2022, Art. no. 20.
- [24] J. Dong et al., "Multiresolution cube propagation for 3-D ultrasound image reconstruction," *IEEE Trans. Comput. Imag.*, vol. 5, no. 2, pp. 251–261, Jun. 2019.
- [25] I. Goodfellow et al., "Generative adversarial nets," in Proc. Adv. Neural Inf. Process. Syst., 2014, vol. 27.
- [26] Y. Zeng, J. Fu, H. Chao, and B. Guo, "Aggregated contextual transformations for high-resolution image inpainting," *IEEE Trans. Vis. Comput. Graph.*, vol. 29, no. 7, pp. 3266–3280, Jul. 2023.
- [27] J. Yu, Z. Lin, J. Yang, X. Shen, X. Lu, and T. S. Huang, "Free-form image inpainting with gated convolution," *Proc. IEEE/CVF Int. Conf. Comput. Vis.*, 2019, pp. 4470–4479.
- [28] G. Xu, W. Liao, X. Zhan, C. Li, X. He, and X. Wu, "Haar wavelet downsampling: A simple but effective downsampling module for semantic segmentation," *Pattern Recognit.*, vol. 143, pp. 109819–109819, Nov. 2023
- [29] C. Wang, B. Chen, Z. Zou, and Z. Shi, "Remote sensing image synthesis via semantic embedding generative adversarial networks," *IEEE Trans. Geosci. Remote Sens.*, vol. 61, 2023, Art. no. 4702811.
- [30] X. Gao, Y. Yao, and Y. Wang, "Reconstruction of global ionospheric TEC maps from IRI-2020 model based on deep learning method," *J. Geodesy*, vol. 98, no. 2, Feb. 2024, Art. no. 10.
- [31] Y. Wen, X. Ma, X. Zhang, and M.-O. Pun, "GCD-DDPM: A generative change detection model based on difference-feature guided DDPM," *IEEE Trans Geosci. Remote Sens.*, vol. 62, 2024, Art. no. 5404416.
- [32] Z. Chen et al., "Improvement of a deep learning algorithm for total electron content maps: Image completion," J. Geophys. Res.: Space Phys., vol. 124, no. 1, pp. 790–800, Jan. 2019.
- [33] E.-Y. Ji, Y.-J. Moon, and E. Park, "Improvement of IRI global TEC maps by deep learning based on conditional generative adversarial networks," *Space Weather*, vol. 18, no. 5, Apr. 2020, Art. no. e2019SW002411.
- [34] Y. Pan, M. Jin, S. Zhang, and Y. Deng, "TEC map completion using DCGAN and poisson blending," *Space Weather*, vol. 18, no. 5, Apr. 2020, Art. no. e2019SW002390.
- [35] J. Chen, H. Fang, and Z. Liu, "The application of a deep convolutional generative adversarial network on completing global TEC maps," *J. Geophys. Res.: Space Phys.*, vol. 126, no. 3, Mar. 2021, Art. no. e2020JA028418.
- [36] Y. Pan, M. Jin, S. Zhang, and Y. Deng, "TEC map completion through a deep learning model: SNP-GAN," *Space Weather*, vol. 19, no. 11, Nov. 2021, Art. no. e2021SW002810.
- [37] D. Yang, H. Fang, and Z. Liu, "Completion of global ionospheric TEC maps using a deep learning approach," J. Geophys. Res.: Space Phys., vol. 127, no. 5, May 2022, Art. no. e2022JA030326.
- [38] Z. Chen, K. Zhou, H. Li, J. Wang, Z. Ouyang, and X. Deng, "Global TEC map fusion through a hybrid deep learning model: RFGAN," Space Weather, vol. 21, no. 1, 2023, Art. no. e2022SW003341.

- [39] J. Matzka, C. Stolle, Y. Yamazaki, O. Bronkalla, and A. Morschhauser, "The geomagnetic Kp index and derived indices of geomagnetic activity," *Space Weather*, vol. 19, no. 5, May 2021, Art. no. e2020SW002641.
- [40] M. Elad, "On the origin of the bilateral filter and ways to improve it," *IEEE Trans. Image Process.*, vol. 11, no. 10, pp. 1141–1151, Oct. 2002.
- [41] B. E. Wood, J. L. Lean, S. E. McDonald, and Y.-M. Wang, "Comparative ionospheric impacts and solar origins of nine strong geomagnetic storms in 2010-2015," *J. Geophys. Res.: Space Phys.*, vol. 121, no. 6, pp. 4938–4965, Jun. 2016
- [42] J. Li, Y. Wang, S. Yang, and F. Wang, "Characteristics of low-latitude ionosphere activity and deterioration of TEC model during the 7–9 september 2017 magnetic storm," *Atmosphere*, vol. 13, no. 9, Aug. 2022, Art. no. 1365.
- [43] D. Chen et al., "Ionospheric irregularities responses to strong geomagnetic torms in Hong Kong region over the past two solar cycles," *IEEE Trans. Geosci. Remote Sens.*, vol. 61, 2023, Art. no. 5604309.



Kunlin Yang received the B.S. degree in electronic science and technology from Xidian University, Xi'an, China, in 2022, and the M.S. degree from the School of Instrumentation and Optoelectronic Engineering, Beihang University, Beijing, P.R. China, in 2025. He is currently working toward with Huawei Technologies Company, Ltd, Shanghai, P.R. China.

His research interests include ionosphere and applications of deep learning in ionosphere.



Yang Liu received the B.S. and Ph.D. degrees from the School of Electronic Information Engineering, Beihang University, Beijing, P.R. China, in 2006 and 2012, respectively.

Since 2012, she has been with CNS/ATM Lab, School of Electronic and Information Engineering, Beihang University. She is with Telecommunications/ICT for Development Laboratory of the International Centre for Theoretical Physics as a one-year visiting scientist in 2017. Currently, she is an Associate Professor with the School of Instrumentation

Science and Optoelectronic Engineering, Beihang University. Her research interests include ionosphere irregularity morphology, ionosphere scintillation, and its effects on GNSS performances.



Zhizhao Liu (Member, IEEE) received the B.Sc. degree in surveying engineering from the Jiangxi University of Science and Technology, Ganzhou, P.R. China, in 1994, the M.Sc. degree in geodesy from Wuhan University, Wuhan, P.R. China, in 1997, and the Ph.D. degree in geomatics engineering from the University of Calgary, Calgary, AB, Canada, in 2004.

He is currently a Professor with the Department of Land Surveying and Geo-Informatics, The Hong Kong Polytechnic University, Hong Kong, P.R. China. He has over 20 years of experience in global

positioning system (GPS)/global navigation satellite system (GNSS) research. His group has developed a highly efficient and effective algorithm of cycle slip detection and repair for dual- and multifrequency GNSS carrier phase data. The algorithm his group developed can improve the accuracy of water vapor retrieval from remote sensing satellite data by up to 50%. His group developed China's first GPS precise point positioning (PPP)-based precipitable water vapor real-time monitoring system in the Pearl-River-Delta region in 2012. In 2012, his group established Hong Kong's first GPS/GNSS-based ionosphere scintillation monitoring system (two stations deployed in South and North Hong Kong) with his collaborators. His research group established Hong Kong's first GPS/GNSS-radiosonde water vapor sounding collocation system in 2013 in collaboration with Hong Kong Observatory. His research interests include new algorithm development for precise GPS and GNSS, GPS/GNSS PPP, ionosphere modeling and scintillation monitoring, tropospheric remote sensing and modeling, and GPS/GNSS meteorology.

Dr. Liu was a recipient of the inaugural Early Career Award of the Hong Kong Research Grants Council (RGC), Hong Kong, in 2012, and the inaugural Best Conference Paper of the China Satellite Navigation Conference (CSNC), China, in 2013. In 2014, he was nominated by Hong Kong Observatory for the World Meteorological Organization (WMO) "Norbert Gerbier-MUMM International Award for 2015" for his paper that has developed a method to evaluate the absolute accuracy of water vapor measurements.



Kaiyan Jin received the M.S. degree from Renmin University of China, Beijing, P.R. China, in 2023. He is currently working toward the doctoral degree with the National Key Laboratory of CNS/ATM, School of Electronic and Information Engineering, Beihang University, Beijing.

He is also the Senior Engineer with the Aviation Data Communication Corporation, ATMB, CAAC, Beijing. His research interests include aeronautical surveillance and airspace safety analysis.



Yifei Chen received the B.S. degree from the Shan-Dong University of Technology, Zibo, China, in 2023. He is currently working toward the postgraduate degree from the School of Instrumentation and Optoelectronic Engineering, Beihang University, Beijing, PR China

His research interests include ionosphere and applications of complex network in ionosphere.



Yanbo Zhu (Member, IEEE) received the B.S. and Ph.D. degrees from Beihang University, Beijing, P.R. China, in 1995 and 2009, respectively.

He is currently the Vice President of the Aviation Data Communication Corporation, Beijing, China. He is also a part-time Professor with the School of Electronic and Information Engineering, Beihang University. His research interests include intelligent air navigation, aeronautical datalink communications, and collaborative air traffic management.